ORNL/SPR-2018/869
Rev. 0

Multi-modal STEM-based tomography of HT-9 irradiated in FFTF

Nuclear Technology Research and Development

Prepared for
U.S. Department of Energy
Advanced Fuels Campaign
K.G. Field, B.P. Eftink,
T.A. Saleh, & S.A. Maloy
Oak Ridge National Laboratory
May 24th, 2018

SUMMARY

Under irradiation, point defects and defect clusters can agglomerate to form extended two and three dimensional (2D/3D) defects. The formation of these defects can be synergistic in nature with one defect or defect-type influencing the formation and/or evolution of another. The result is a need exists to perform advanced characterization where microstructures are accurately reproduced in 3D. Here, HT-9 neutron irradiated in the Fast Flux Test Facility (FFTF) was used to evaluate the ability of multi-tilt STEM-based tomography to reproduce the fine-scale radiation-induced microstructure in 3D. High-efficiency STEM-EDS was used to provide both structural and chemical information during the 3D reconstruction. The results show similar findings to a previous two-tilt tomography study on the same material; the α' phase is denuded around the Ni-Si-Mn rich G-phase and cavities. It is concluded both tomography reconstruction techniques (two-tilt and multi-tilt) are readily viable for advanced 3D characterization of irradiated materials and could add significant value to the advanced characterization capabilities for nuclear materials development.

CONTENTS

FIGURES

ACRONYMS

2D	Two-dimensional
3D	Three-dimensional
BF	Bright-field
DOE	Department of Energy
dpa	displacements per atom
EDS	Electron-Dispersive X-ray Spectroscopy
FFTF	Fast Flux Test Facility
FIB	Focused Ion Beam
F/M	Ferritic/Martensitic
HAADF	High angle annular dark field
LAADF	Low angle annular dark field
LAMDA facility	Low Activation Materials Development & Analysis Facility
LANL	Los Alamos National Laboratory
MAADF	Medium angle annular dark field
N/A	Not Applicable
N/O	Not Observed
NTRD	Nuclear Technology Research & Development
ORNL	Oak Ridge National Laboratory
PIE	Post-Irradiation Examination
RIS	Radiation-induced segregation
SDD	Silicon-Drift Detector
SEM	Scanning Electron Microscopy
STEM	Scanning Transmission Electron Microscopy
TEM	Transmission Electron Microscopy

MULTI-MODAL STEM-BASED TOMOGRAPHY OF HT-9 IRRADIATED IN FFTF

1. INTRODUCTION

Neutron irradiation damage in candidate cladding alloys for high dose applications, such as high chromium (>8 wt.% Cr) body centered cubic (BCC) ferritic/martensitic (F/M) steels, will result in the formation of point defects (interstitials and/or vacancies) and small vacancy and interstitial clusters. At typical reactor temperatures (300-500°C) these defects can diffuse, annihilate, or agglomerate resulting in the formation of extended two-dimensional (2D) and three-dimensional (3D) defects. For high chromium F/M steels, such as HT-9, these extended defects can include but are not limited to dislocation loops, cavities/bubbles/voids, Ni-Si-Mn rich phases such as G-phase, and radiation-induced segregation (RIS) [1–4]. The nucleation and growth of these extended defects depends on a range of factors including irradiation temperature, dose, and dose rate among others [5]. Furthermore, the evolution of the defects tends to be interrelated, defects can interact with each other or the progression of RIS can lead to radiation-induced precipitation (RIP). This complex, correlated microstructural evolution occurs in 3D and thus the highest fidelity understanding on the microstructural evolution and radiation tolerance of a given material requires 3D post-irradiation examination (PIE) techniques.

The ability to conduct 3D characterization using tomography-based techniques in materials science has rapidly progressed in recent years with the advent of computerized system controls and advancements in tomography reconstruction software [6–8]. Given this, the progression of using tomography techniques for the characterization of irradiated materials remains limited. The *de facto* technique to date is atom probe tomography (APT). APT is a destructive analysis technique that uses field evaporation and a position-sensitive detector and a time-of-flight detector to identify the original location and determine the chemical identity of each atom which is the reconstructed to form a 3D tomographic chemical image of the specimen. The APT technique is immensely powerful for irradiated materials and has been used in a range of applications including looking at nano-cluster stability in nanostructured ferritic alloys [9,10], determining the formation and precipitation of the α' phase in FeCrAl alloys [11,12], and analyzing radiation-induced segregation (RIS) in F/M steels [13], among many others. However, APT datasets are subject to aberration artifacts, the analysis is performed on very small sample volumes (10^{-22} to 10^{-21} m^3 per sample), and determination of the spatial-correlation between structural defects is strongly dependent on there being chemical signatures associated with them (e.g. segregation of minor alloying elements to dislocation loops).

Scanning transmission electron microscopy (STEM)-based tomography has been growing in popularity in the past decade due to recent advances in digital data collection as well as the advent of high brightness sources and being outfitted with the latest generation of large-collection angle, high efficiency energy dispersive X-ray dispersive spectroscopy (EDS) spectrometers. STEM-based techniques can have much larger sample volumes compared to APT and produces 3D reconstructions from a series of 2D projected images acquired at various tilt angles. These 2D images, and hence the tomographic image, can be inherently multi-modal due to the simultaneous collection of different scattering contrast images and the collection of EDS map images. The result is a distinct advantage over APT as both the chemical and structural data can be reconstructed in a single volume during a single experiment when using STEM-EDS-based tomography. Such advantage is uniquely positioned to provide detailed insight into the production of irradiated microstructures in a range of alloy and material classes.

Over the past two years, the Nuclear Technology Research & Development (NTRD) program for the Department of Energy (DOE) has been investigating the application of STEM-based tomography to perform high-fidelity characterization of neutron irradiated candidate cladding alloys to both explore the power of the technique and further refine theories on the radiation tolerance of the studied alloys. The

primary alloy of interest for these studies has been the F/M steel, HT-9. HT-9 is a high chromium (>8 wt.% Cr) BCC F/M steel used within the fossil fuel and nuclear industry for structural steel and fast reactor cladding applications [14]. The microstructure consists of a complex array of grains/grain boundaries including prior austenite grain boundaries, packet boundaries, and lath/lath boundaries. In the as-received state, the matrix is also populated with a variety of precipitates including inter- and intra-granular $M_{23}C_6$ carbides and intra-granular MX precipitates. A high number density of line dislocations will also be present in the microstructure. This highly complex microstructure results in enhanced radiation tolerance, especially swelling resistance, in high dose cladding applications [15]. The excellent swelling resistance has also led to further studies within the DOE NTRD program to investigate the applicability of additive manufacturing techniques for HT-9 [16]. Neutron irradiated HT-9 is ideally suited for STEM-based tomography investigations as both structural and chemical changes occur under irradiation. Previously, the application of a two-tilt STEM-tomography technique was studied for a HT-9 specimen neutron irradiated in the Fast Flux Test Facility (FFTF) to a dose of 155 displacements per atom (dpa) at 443°C [3]. The heat of HT-9 was Heat 84425 which composed the AC0-3 duct [2–4]. The previous study [17] which used the obtain3D software [18] showed the synergistic nature between the radiation-induced/enhanced α', G-phase, and cavities and the strength of two-tilt technique. Here, the previous work is extended to investigate both the chemical changes (α' and G-phase) and the structural changes (line dislocations, dislocation loops, and cavities) using a multi-tilt reconstruction technique.

2. METHODS

2.1 STEM-based experiments

Bulk neutron irradiated HT-9 was obtained from Los Alamos National Laboratory (LANL) as part of a prior tomography study. The conditions obtained are listed in Table 1. Previously, focused ion beam (FIB) prepared STEM transparent lamellae were fabricated and investigated from condition 5A1. In an effort to expand not only the characterization technique but the library of suitable conditions with STEM transparent lamellae, additional FIB prepared STEM transparent lamellae were extracted from condition 6A1. For both conditions, lamellae were prepared using FEI Quanta 3D DualBeam Focused Ion Beam-Scanning Electron Microscope (FIB-SEM) from 1 mm discs from shear-punch tests. Primary specimen trenching and thinning was completed using a 30 kV Ga^+ ion beam with specimens being thinned to final conditions using a 2 kV, 48-72 pA Ga^+ ion beam on the FEI Quanta 3D DualBeam FIB-SEM.

Table 1: Summary of HT-9 samples that were irradiated in FFTF and obtained for characterization at ORNL.

Sample ID	Damage Dose (dpa)	Temp. (°C)	# FIB-prepared samples	2D Characterization	2-tilt Tomography	Multi-tilt Tomography
4A1	110	470	1	×		
5A1	155	450	3	×	×	×
6A1	15	370	2	×		
6A5	115	420	0			

*×: denotes activity completed

Key to the tomography experiments is the application of the high-efficiency STEM-EDS which is capable of rapidly producing multi-modal data. The FEI Talos F200X S/TEM instrument is ideally suited for such experiments due to its high brightness electron beam, four silicon-drift detector (SDD) X-ray detectors (total of 0.9 srad of collection angle), and four image detectors (bright field (BF), low-angle annular dark field (LAADF), medium angle annular dark field (MAADF) and high-angle annular dark field (HAADF)). The FEI F200X S/TEM housed in the Low Activation Materials Development and Analysis

(LAMDA) facility at Oak Ridge National Laboratory (ORNL) was used for this study. For each STEM investigation both BF/LAADF/MAADF/HAADF image quadruplets (1024×1024 pixels) and EDS spectrum data cubes (1024×1024 pixels, 3 nA probe) were acquired. The EDS spectrum data cube-image pair acquisition was controlled using Bruker's Quantax Esprit software. Additionally, Kikuchi diffraction patterns were acquired to determine the crystallographic orientation for acquisitions associated with 3D tomography experiments.

2.2 Tomographic reconstructions

At first, the 6A1 condition was initially explored for STEM-based experiments, but the specimens showed no significant radiation-induced defects when imaged in typical 2D projections negating the need for high-fidelity tomography experiments. The result was tomography-based experiments were again focused on the 5A1 specimen as the microstructure proved to be complex and warranted further high-fidelity tomography characterization. The tomography data acquisition on the 5A1 specimen was conducted with a constant non-eucentric tilt of 1.26° and varying eucentric tilt in the range of -40° to +40°. The tilt configurations were setup to image a region of interest where the full tilt range acquired images with a constant diffraction condition of $\mathbf{g}\approx200$; several orientations were acquired near or at a zone axis including the [100] zone axis. STEM-based diffraction contrast imaging is capable of imaging both line dislocations and dislocation loops in a single micrograph [19,20] where the $\mathbf{g}\approx200$ condition can image loops with Burgers vectors of ½[111], ½[-111], ½[1-11], ½[11-1], and [001] [21]. BF/LAADF/MAADF/HAADF image quadruplets were acquired at 1° eucentric tilt increments for the full tilt range while EDS spectrum cubes were acquired at 5° eucentric tilt increments in the range of -30° to +30°. 60-minute acquisition time/maps were acquired for the tilt of 0°/1.26° (eucentric/non-eucentric) and -15°/1.26°; all other maps were acquired for 15 minutes. EDS count maps from the Bruker Quantax Esprit software were exported as 16-bit tiff maps. Due to the generally low acquisition time (15 minutes), the raw count maps were sparse datasets. In an effort to increase the detection of radiation-induced defects, especially the formation of the Cr-rich α' phase, a macro was built for ImageJ [22,23] to perform post-acquisition image processing. The code is provided in Figure 1 and the image after each processing step is shown in Figure 2.

Tomographic reconstructions were produced using ImageJ. The LAADF image, the $Cr_{K\alpha,}$ and the $Ni_{K\alpha}$ maps were combined to form Magenta, Yellow, Cyan (respectively) composite maps prior to final reconstructions for the 5° increment tilt-series. The LAADF image was used for the 1° increment tilt series. Final contrast adjustments were completed using the "Stack Contrast Adjustment" plugin for ImageJ with tilt-axis corrections completed using the "Linear Stack Alignment with SIFT" plugin. Tilt-stacks were exported as animated GIFs to readily provide a 3D perspective to the reconstructions. Software such as FEI's Amira-Avizo 3D software suite was not applied for the preliminary nature of this work, but future activities seeks to include use of such software to provide more robust tomographic reconstructions. Animated gifs were produced with 4 frames/s for the tilt series with 5° increments and at 12 frames/s for tilts series with 1° increments.

```
1  run("Bin...", "x=2 y=2 bin=Average");
2  run("Enhance Contrast...", "saturated=0.3 normalize equalize");
3  run("Bandpass Filter...", "filter_large=50 filter_small=1 suppress=None tolerance=5 autoscale
4  saturate");
5  title = getTitle();
6  dir = getDirectory("image");
7  saveAs("Jpeg", dir+title+"process");
```

Figure 1: Post-acquisition image processing code used in ImageJ for tomographic reconstruction of the STEM-EDS count maps.

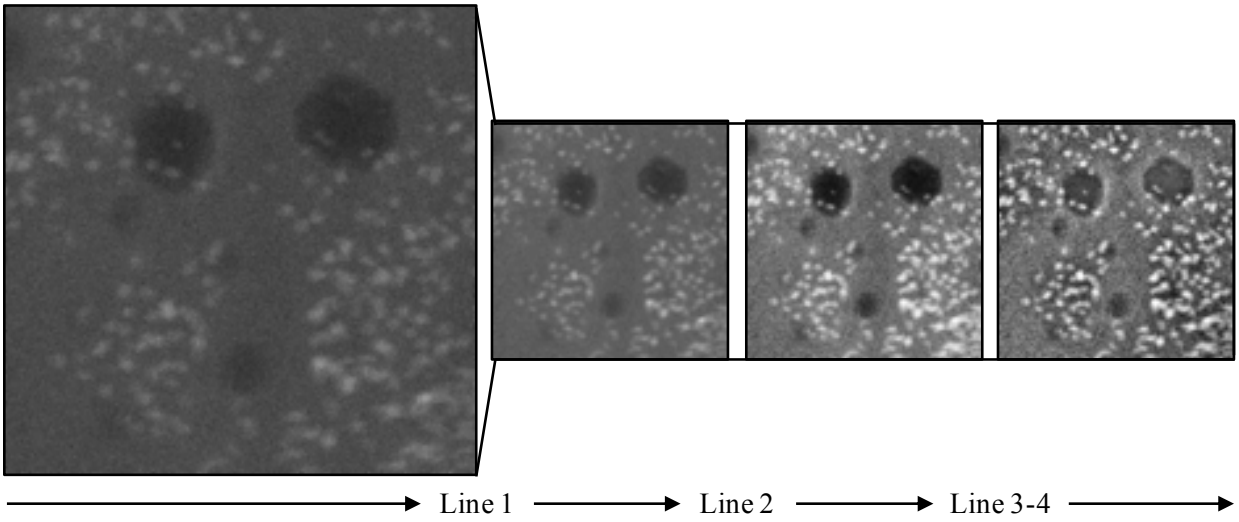

Figure 2: Raw $Cr_{K\alpha}$ map from neutron irradiated HT-9 followed by post-processing steps in ImageJ provided in Figure 1; labels designation code line. Final image (right) was used for tomographic reconstructions. Image taken at tilt of 0°/1.26° with 1 hr acquisition time. Image scale: 336×336 nm.

3. RESULTS AND DISCUSSION

3.1 2D representation of the microstructure for condition 6A1 and 5A1

Figure 3 shows the radiation-induced microstructure from the 6A1 condition sample of HT-9 (15 dpa, 370°C). The microstructure shows the typical lath structure of HT-9 as well as the typical precipitate/carbide structure. Figure 3 shows limited radiation-induced microstructural features which is further corroborated at higher magnification shown in Figure 4. No presence of cavities, G-phase, or the Cr-rich α' is observed, suggesting that the lower irradiation dose (15 dpa) has not provided for the formation of such features. Some Ni-enrichment is observed at grain boundaries, but without a reference unirradiated sample it is impossible to determine if the observed segregation is pre-existing or RIS. Table 2 compares the observations from this study to those of Anderoglu et al. [2], Sencer et al. [3,4], and the recent confirmatory study completed by Woodley [24]. The observations for this irradiation condition are inconsistent with that of Anderoglu et al. [2] where both G-phase (Ni-Si-Mn rich phase) and the Cr-rich α' phase was observed in specimens extracted from a region of HT-9 irradiated to 20 dpa at 380°C. The variance could be the result of limited sample volume conducted within this study and/or the specimen thickness reducing resolution below that of the fine scaled particles. Further investigations, such as a round-robin testing, are suggested to evaluate the variance in the observed microstructure in this study compared to that conducted within Anderoglu et al. [2]. The 6A1 specimen was not selected for further tomography studies due to the limited degree of radiation-induced fine structure.

Figure 5 shows the radiation-induce microstructure from the 5A1 condition sample of HT-9 (155 dpa, 450°C). The observed microstructure is identical to that observed in the previous tomography study [17], Anderoglu et al. [2], and by Woodley [24], Table 2. The microstructure is inherently complex with G-phase precipitates which are rich in Ni, Si, and Mn on the order of 25-50 nm, a mixed size distribution of cavities/voids, the formation of nanoscale (5-15 nm) Cr-rich α', the presence of both ½⟨111⟩ and ½⟨111⟩

dislocation loops and line dislocations. The loop density was observed to be quite low, with only several loops imaged in a typical areal size of 0.1 μm^2. The α' density is quite high, most likely due to a thicker specimen region than previously observed, and at first observation a denuded zone appears to be present around the G-phase particles and the cavities.

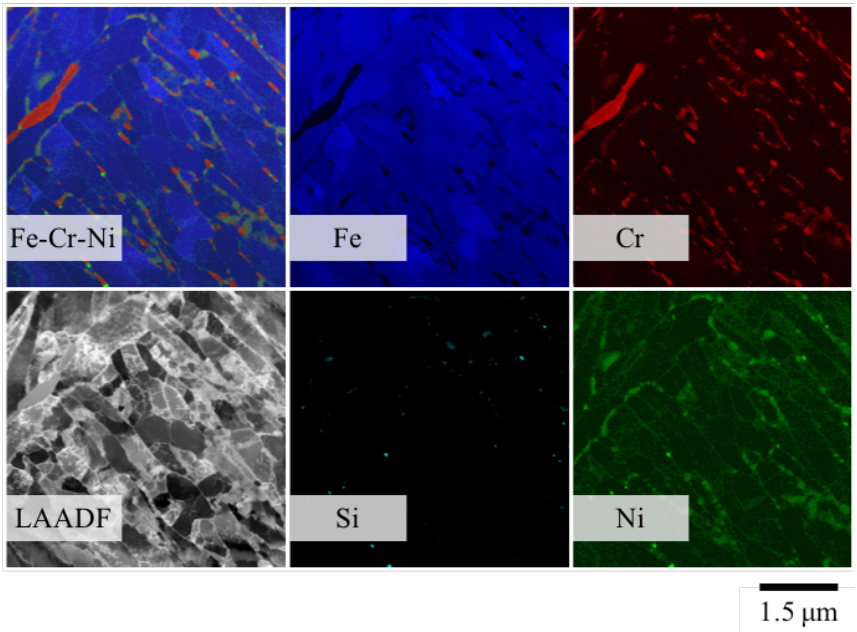

Figure 3: 2D projections of the 3D volume from HT-9 neutron irradiated to 15 dpa at 370°C. Images taken at low magnification to show general structure of the alloy, Cr-rich carbides and Ni-rich precipitates are observed.

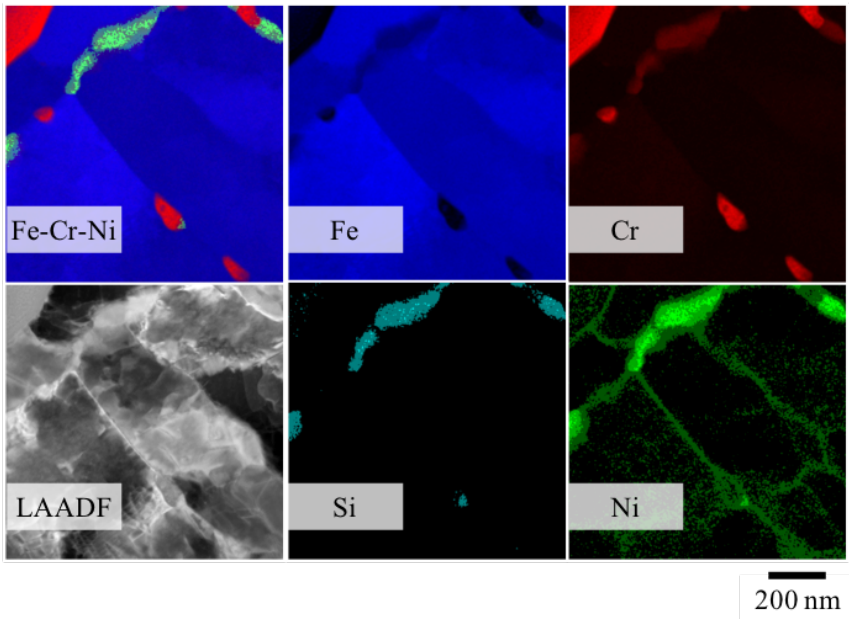

Figure 4: 2D projections of the 3D volume from HT-9 neutron irradiated to 15 dpa at 370°C. Images taken at higher magnification than Figure 3 to determine the presence of G-phase and/or Cr-rich α'.

Table 2: Summary of observed radiation-induced defects in neutron irradiated HT-9 across multiple studies

Condition	Defect		Anderoglu [2]	Sencer et al. [3,4]	This study & Ref. [17]	Woodley [24]
466-470 °C 92-110 dpa (4A1)	Cavities	Size (nm)	~30	-	N/O	-
		Density (m^{-3})	N/A	-	N/O	-
	Loops	Size (nm)	N/A	-	N/O	-
		Density (m^{-3})	N/A	-	N/O	-
	α'	Size (nm)	N/O	-	N/O	-
		Density (m^{-3})	N/O	-	N/O	-
	G-phase	Size (nm)	N/O	-	N/O	-
		Density (m^{-3})	N/O	-	N/O	-
440-450 °C 150-155 dpa (5A1)	Cavities	Size (nm)	28	28	O	24 ± 1
		Density (m^{-3})	2.5×10^{20}	2.5×10^{20}	O	2.9×10^{20}
	Loops	Size (nm)	18	18	O	O
		Density (m^{-3})	$\sim 5 \times 10^{20}$	$\sim 5 \times 10^{20}$	O	O
	α'	Size (nm)	9.6 ± 1.9	O	N/A	O
		Density (m^{-3})	1.1×10^{21}	O	N/A	O
	G-phase	Size (nm)	26.5 ± 5.7	~22	O	25 ± 1
		Density (m^{-3})	1.1×10^{21}	$\sim 10 \times 10^{20}$	O	2.4×10^{20}
370-384 °C 15-28 dpa (6A1)	Cavities	Size (nm)	N/O	N/A	N/O	-
		Density (m^{-3})	N/O	N/A	N/O	-
	Loops	Size (nm)	N/A	~14	N/O	-
		Density (m^{-3})	N/A	$\sim 9.3 \times 10^{20}$	N/O	-
	α'	Size (nm)	7.8 ± 1.2	N/A	N/O	-
		Density (m^{-3})	7.2×10^{22}	N/A	N/O	-
	G-phase	Size (nm)	11.3 ± 2.3	~8.5	N/O	-
		Density (m^{-3})	9.3×10^{21}	4.5×10^{21}	N/O	-
410-420 °C 100-115 dpa (6A5)	Cavities	Size (nm)	18	-	-	-
		Density (m^{-3})	7.5×10^{19}	-	-	-
	Loops	Size (nm)	N/A	-	-	-
		Density (m^{-3})	N/A	-	-	-
	α'	Size (nm)	8.8 ± 1.3	-	-	-
		Density (m^{-3})	2.2×10^{22}	-	-	-
	G-phase	Size (nm)	16 ± 3.1	-	-	-
		Density (m^{-3})	3.2×10^{21}	-	-	-

*N/O: Not observed; O: Observed; N/A: Not applicable; - : Not studied

The similarities in the region of interest for condition 5A1 in this study and the previous two-tilt study [17,18] on the same irradiation condition suggests that a reasonable comparison can be made between the two techniques. In addition, the same microscope and magnifications were used to provide direct comparisons in the ability for the two techniques to provide representations of the 3D microstructure through tilt-series of the 2D projection. Of particular interest is whether both techniques observed any synergies between the Cr-rich α' and the other radiation-induced microstructural features. To evaluate the difference between the two-tilt and multi-tilt techniques a series of reconstructions were generated from the region-of-interest in Figure 5 using the multi-tilt technique.

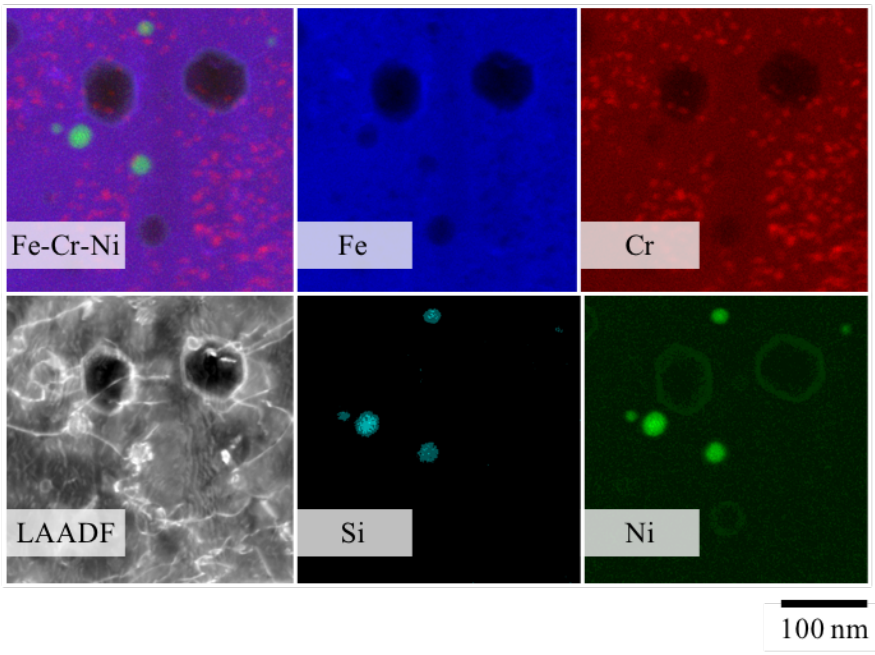

Figure 5: 2D projections of the 3D volume from HT-9 neutron irradiated to 155 dpa at 450°C. images show the presence of G-phase, Cr-rich α', cavities, and dislocation loops.

3.2 3D representation of the microstructure for condition 5A1

Two different 3D reconstructions were generated. The first being a reconstruction (Reconstruction #1) of the diffraction-based STEM contrast (LAADF) at a tilt range of -40° to 40° at 1° increments and the second (Reconstruction #2) being the STEM-based EDS and diffraction contrast taken at a tilt range of -30° to 30° at 5° increments. The two reconstructions were done to evaluate whether sparser tilt series could provide representative constructions from the higher fidelity tilt series. Reconstruction #1 was only completed on the LAADF signal as acquiring EDS signals over eighty different unique tilts would be prohibitively time consuming.

The images comprising Reconstruction #1 are shown in Figure 6. Dislocation loops of both ½⟨111⟩ and ⟨100⟩ type, line dislocations threading from the free surfaces, G-phase, and large and small cavities are all observable within the reconstruction. The Cr-rich α' is not observable as the similar lattice parameters between the precipitates and the matrix [25] prevents diffraction-based contrast imaging. The high-fidelity of the data series provides a robust reconstruction. For example, Figure 7 shows ½⟨111⟩ dislocation loops associated with a large void at -30° but it becomes apparent at +30° the dislocation loop is not associated with the void at all. Line dislocations are observed to intersect the free surface as well as show intersections/interactions with other microstructure defects such as G-phase. The ability to maintain diffraction contrast over the entire tilt-series is remarkable and shows the power of STEM-based diffraction contrast imaging. A primary downfall of the dataset is the modal artifact contrast within the images. The 3D reconstruction shows these artifacts are representative of the free surface and most likely a surface oxide or other non-representative feature of the irradiated microstructure.

The multi-modal reconstruction of Reconstruction #2 provides even more detail regarding the fine microstructure within the sample. Figure 8 shows the images used to compose the reconstruction. The most apparent observation is the Cr-rich α' phase is readily observable in the $Cr_{k\alpha}$ count maps and a Ni-Cr enrichment exists on the large void surface. Excerpts from the full reconstruction, Figure 9, shows that the Cr-rich α' is denuded around G-phase (yellow) and the cavities within the region of interest leading to a

"spotty" decoration of α' within the microstructure. Denudation of Cr-rich α' was observed in prior two-tilt reconstructions [17,18] but what was not revealed was the additional denudation near the ½⟨111⟩ loops within microstructure while line dislocations showed no denuded regions of α'. This observation suggests a competition between the production of cavities and voids with Cr-rich α' but none exists for the assumed pre-existing line dislocations under irradiation.

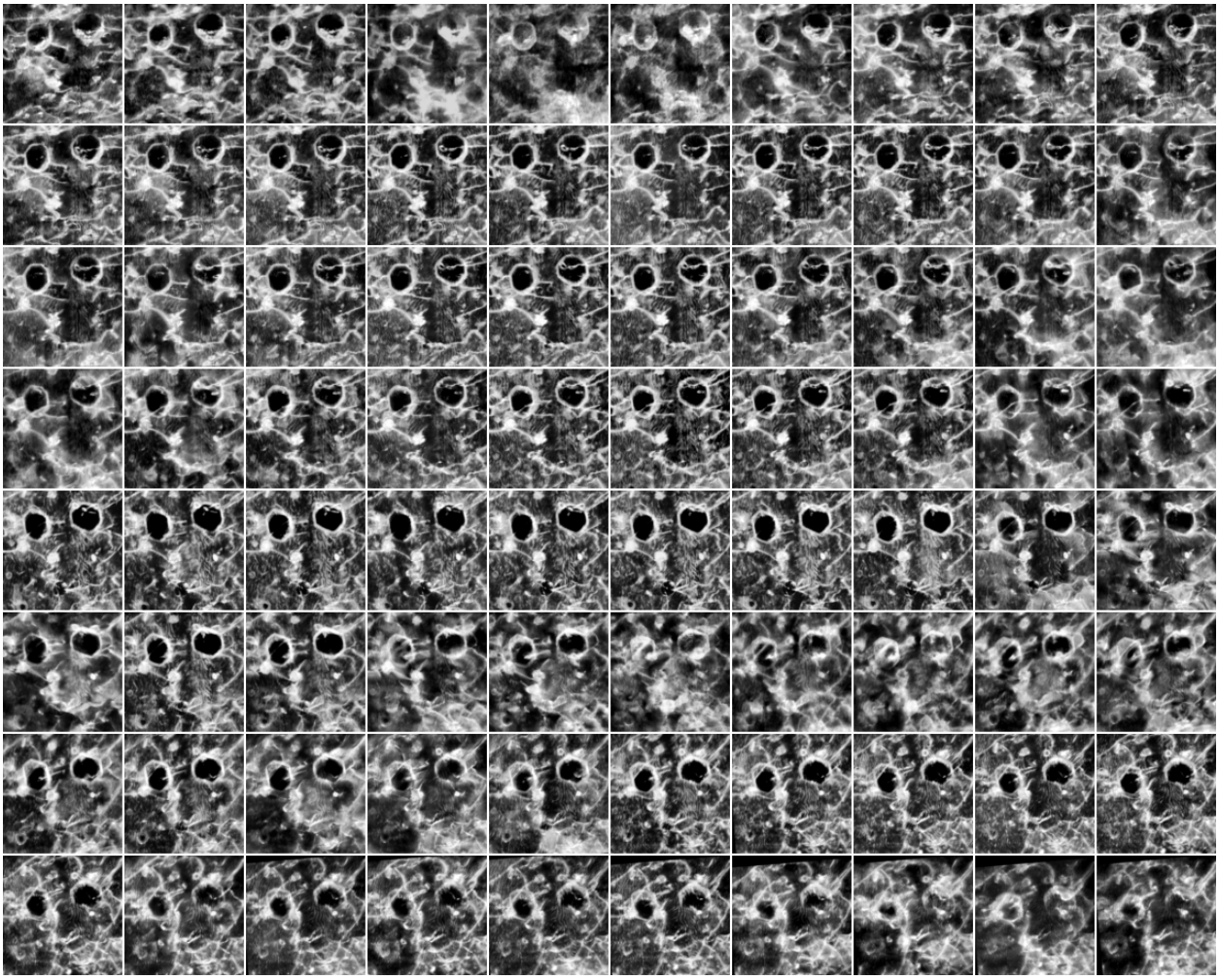

Figure 6: Image montage at varying specimen tilts LAADF taken at 1° increments from 40° to -40°C in a left-to-right, top-down fashion. Individual image scale: 336×336 nm.

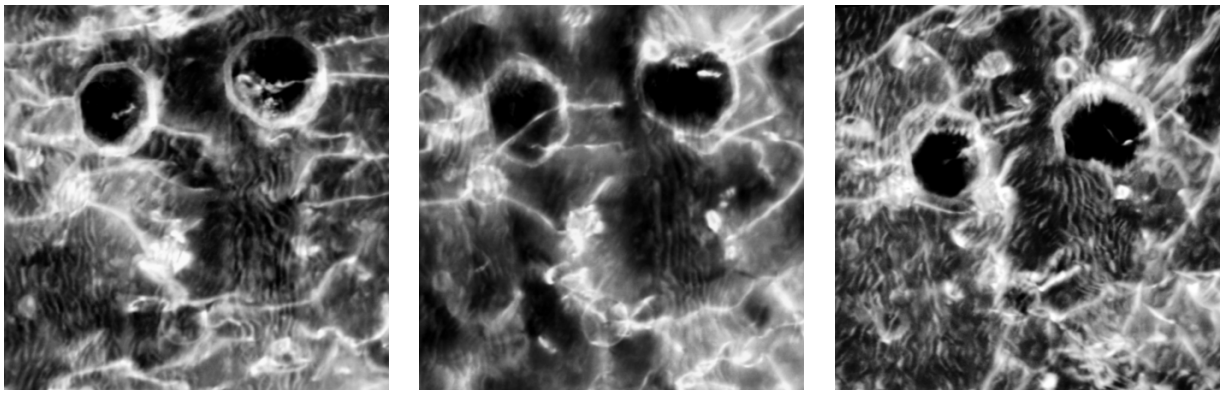

Figure 7: LAADF images at varying specimen tilts showing the spatial correlation of voids and line dislocations, and dislocation loops in HT-9 irradiated to 155 dpa at 450°C.

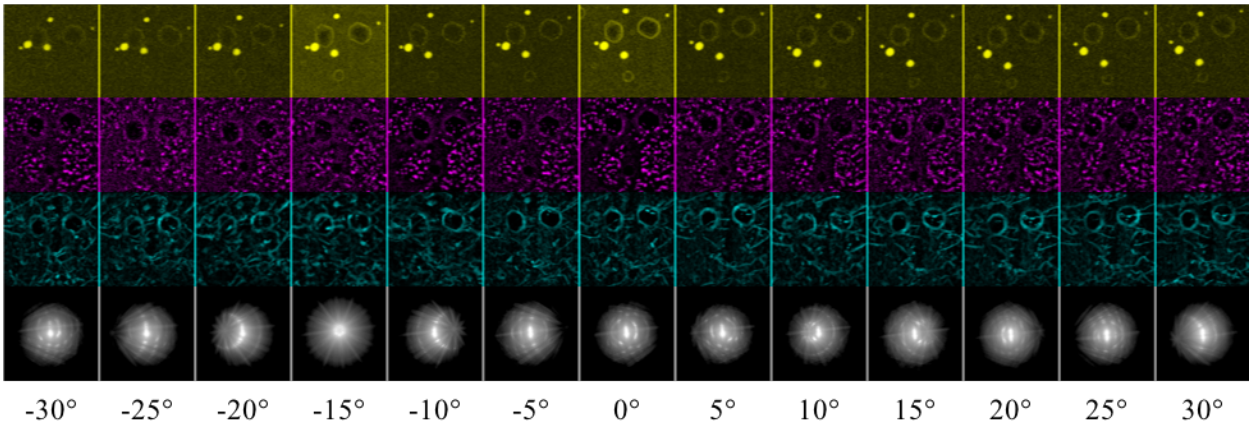

Figure 8: Image montage at varying specimen tilts of $Ni_{K\alpha}$ (yellow), $Cr_{K\alpha}$ (magenta), LAADF (cyan) used to form the tomographic reconstruction. Image scale: 336×336 nm. Kikuchi pattern (gray-scale) shown to provide insight on imaging conditions.

The relative ease in which to produce accurate 3D representations of the irradiated microstructure using high-efficiency STEM-EDS makes a strong case for its use in future advanced characterization activities within the DOE NTRD program. Some inherent flaws are present in the STEM-EDS tomographic techniques. First off, the Cr-rich α', being a nanoscale cluster embedded in the matrix, is difficult to observe even using a high-efficiency STEM-EDS. As the foil is tilted, it became apparent that α' clusters near the foil bottom had sparser/less statistically significant $Cr_{k\alpha}$ signatures compared to those near the foil top due to absorption effects – this is especially apparent in STEM-EDS mapping taken with 15-minute acquisition times (where top is orientated closer to the electron gun of the system). Strong definition of the α' clusters' morphology when positioned near the foil bottom is difficult, if not impossible to achieve using the configurations within this study. This effect is easy to overcome; one can investigate thinner specimen regions less prone to absorption effects and/or generate maps with acquisition times longer than 15 minutes. An additional flaw of the proposed technique is the low spatial-tilt resolution when 5° tilt increments are used. Compared to Reconstruction #1, Reconstruction #2 still produces gross variants within 3D space but finer spatial variants (<10-20 nm) becomes more difficult to discern. Again, this is easy to overcome by decreasing the tilt increment below 5° but this results in large

STEM-EDS session times and thus a decision needs to be made between data fidelity and session time/cost.

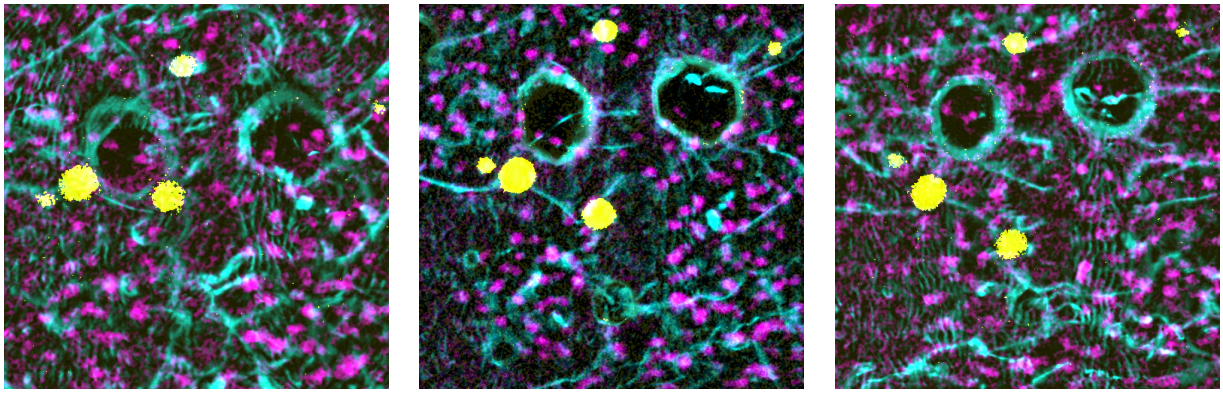

-30° 0° 30°

Figure 9: Composite images at varying specimen tilts showing the spatial correlation of G-phase (yellow), Cr-rich α' (magenta), voids (cyan), dislocation loops (cyan) and line dislocation (cyan) in HT-9 irradiated to 155 dpa at 450°C.

In general, both the multi-tilt reconstructions in this work and the two-tilt reconstructions in the previous work provided the same observations regarding the radiation-induced microstructure in the 5A1 condition of the HT-9 specimens irradiated in the FFTF. Both show denudation of Cr-rich α' at other radiation-induced microstructural features. Given this, the multi-tilt reconstruction showed also the non-synergistic nature between the dislocation loops and the α'. This ability is not unique to the multi-tilt technique, the two-tilt technique could produce the same respective reconstructions if the initial images taken in the previous study were conducted with the image condition remaining constant with $\mathbf{g}\approx200$. Based on the observations both techniques can be recommended for use in the 3D characterization of irradiated microstructure for DOE NTRD program activities. Several factors should be considered when deciding the technique to be used including that the two-tilt technique [17,18] requires significantly less acquisition time on the microscope but could have difficulties discerning complex curvatures, a problem not observed here due to do the relatively spherical nature of the defects observed.

4. CONCLUSIONS

Neutron irradiated HT-9 specimens were used to conduct multi-modal STEM-based tomography for the purpose of evaluating the technique as a complementary technique to currently used tomography techniques such as APT. The complex, fine-scaled microstructure of the HT-9 specimen in the 5A1 condition (155 dpa, 443°C) was ideally suited to conduct the study. The multi-tilt reconstruction provided identical observations to that of the previously conducted two-tilt reconstructions with the most significant finding being that α' remains denuded around the Ni-Si-Mn-rich G-phase precipitates. The multi-tilt reconstructions are microscopy-intensive, requiring significant equipment time to generate sufficient statistically significant data in spectrum images at fine tilt increments at wide tilt ranges. Further studies are needed to refine the data-acquisition configurations to optimize the data collection and tomography reconstructions. Given this, both tilt-techniques are straightforward to accomplish and should be readily pursued for advanced characterization capabilities within the NTRD.

5. ACKNOWLEDGEMENTS

The work presented in this report was supported by the Advanced Fuels Campaign of the Nuclear Technology R&D program in the Office of Nuclear Energy, US Department of Energy. This research was performed using instrumentation (FEI Talos F200X S/TEM) provided by the Department of Energy, Office of Nuclear Energy, Fuel Cycle R&D Program and the Nuclear Science User Facilities. The authors would like to thank T.J. Romero and M. Quintana for supplying the neutron irradiated HT-9 for this study. The authors are indebted to M.B. Toloczko, B. Makenas and W. Witherspoon of Pacific Northwest National Laboratory for the information describing the irradiation conditions of the AC0-3 duct and who led the retrieval of this duct for analysis.

6. REFERENCES

[1] R.L. Klueh, Miniature tensile test specimens for fusion reactor irradiation studies, Nucl. Eng. Des. Fusion. 2 (1985) 407–416. doi:10.1016/0167-899X(85)90028-X.

[2] O. Anderoglu, J. Van den Bosch, P. Hosemann, E. Stergar, B.H. Sencer, D. Bhattacharyya, R. Dickerson, P. Dickerson, M. Hartl, S.A. Maloy, Phase stability of an HT-9 duct irradiated in FFTF, J. Nucl. Mater. 430 (2012) 194–204. doi:10.1016/j.jnucmat.2012.06.038.

[3] B.H. Sencer, J.R. Kennedy, J.I. Cole, S.A. Maloy, F.A. Garner, Microstructural analysis of an HT9 fuel assembly duct irradiated in FFTF to 155dpa at 443°C, J. Nucl. Mater. 393 (2009) 235–241. doi:10.1016/j.jnucmat.2009.06.010.

[4] B.H. Sencer, J.R. Kennedy, J.I. Cole, S.A. Maloy, F.A. Garner, Microstructural stability of an HT-9 fuel assembly duct irradiated in FFTF, J. Nucl. Mater. 414 (2011) 237–242. doi:10.1016/j.jnucmat.2011.03.050.

[5] O. Anderoglu, T.S. Byun, M. Toloczko, S.A. Maloy, Mechanical Performance of Ferritic Martensitic Steels for High Dose Applications in Advanced Nuclear Reactors, Metall. Mater. Trans. A. 44 (2013) 70–83. doi:10.1007/s11661-012-1565-y.

[6] W. Guo, B.T. Sneed, L. Zhou, W. Tang, M.J. Kramer, D.A. Cullen, J.D. Poplawsky, Correlative Energy-Dispersive X-Ray Spectroscopic Tomography and Atom Probe Tomography of the Phase Separation in an Alnico 8 Alloy, Microsc. Microanal. 22 (2016) 1251–1260. doi:10.1017/S1431927616012496.

[7] C. Kübel, A. Voigt, R. Schoenmakers, M. Otten, D. Su, T.-C. Lee, A. Carlsson, J. Bradley, Recent Advances in Electron Tomography: TEM and HAADF-STEM Tomography for Materials Science and Semiconductor Applications, Microsc. Microanal. 11 (2005) 378–400. doi:10.1017/S1431927605050361.

[8] J. Kacher, G.S. Liu, I.M. Robertson, In situ and tomographic observations of defect free channel formation in ion irradiated stainless steels, Micron. 43 (2012) 1099–1107. doi:10.1016/j.micron.2012.01.017.

[9] A.G. Certain, K.G. Field, T.R. Allen, M.K. Miller, J. Bentley, Response of nanoclusters in nanostructured ferritic alloys to low-dose proton irradiation, in: Trans. Am. Nucl. Soc., 2010.

[10] A. Certain, S. Kuchibhatla, V. Shutthanandan, D.T. Hoelzer, T.R. Allen, Radiation stability of nanoclusters in nano-structured oxide dispersion strengthened (ODS) steels, J. Nucl. Mater. 434 (2013) 311–321. doi:10.1016/j.jnucmat.2012.11.021.

[11] S.A. Briggs, P.D. Edmondson, K.C. Littrell, Y. Yamamoto, R.H. Howard, C.R. Daily, K.A. Terrani, K. Sridharan, K.G. Field, A combined APT and SANS investigation of α′ phase precipitation in neutron-irradiated model FeCrAl alloys, Acta Mater. 129 (2017) 217–228.

doi:10.1016/j.actamat.2017.02.077.

[12] P.D. Edmondson, S.A. Briggs, Y.Yamamoto, R.H. Howard, K. Sridharan, K.A. Terrani, K.G. Field, Irradiation-enhanced α′ precipitation in model FeCrAl alloys, Scr. Mater. 116 (2016) 112–116. doi:10.1016/j.scriptamat.2016.02.002.

[13] Z. Jiao, S. Taller, K. Field, G. Yeli, M.P. Moody, G.S. Was, Microstructure evolution of T91 irradiated in the BOR60 fast reactor, J. Nucl. Mater. 504 (2018). doi:10.1016/j.jnucmat.2018.03.024.

[14] R.L. Klueh, D.R. Harries, High-chromium ferritic and martensitic steels for nuclear applications, ASTM, 2001.

[15] E. Getto, K. Sun, A.M. Monterrosa, Z. Jiao, M.J. Hackett, G.S. Was, Void swelling and microstructure evolution at very high damage level in self-ion irradiated ferritic-martensitic steels, J. Nucl. Mater. 480 (2016) 159–176. doi:10.1016/j.jnucmat.2016.08.015.

[16] N. Sridharan, K.G. Field, Preliminary Characterization and Mechanical Performance of Additively Manufactured HT9, ORNL/SPR-2018/7802. (2018).

[17] K.G. Field, B.P. Eftink, C.M. Parish, T.A. Saleh, S.A. Maloy, Synergies Between α' and Cavity Formation in HT-9 Following High Dose Neutron Irradiation, ORNL/TM-2017/274. (2017).

[18] B.P. Eftink, S.A. Maloy, obtain3D, (2017). https://www.osti.gov/servlets/purl/1371737.

[19] P.J. Phillips, M.C. Brandes, M.J. Mills, M. De Graef, Diffraction contrast STEM of dislocations: imaging and simulations, Ultramicroscopy. 111 (2011) 1483–1487. doi:10.1016/j.ultramic.2011.07.001.

[20] C.M. Parish, K.G. Field, A.G. Certain, J.P. Wharry, Application of STEM characterization for investigating radiation effects in BCC Fe-based alloys, J. Mater. Res. 30 (2015) 1246–1274. doi:10.1557/jmr.2015.32.

[21] B. Yao, D.J.J. Edwards, R.J.J. Kurtz, TEM characterization of dislocation loops in irradiated bcc Fe-based steels, J. Nucl. Mater. 434 (2013) 402–410. doi:10.1016/j.jnucmat.2012.12.002.

[22] C.A. Schneider, W.S. Rasband, K.W. Eliceiri, NIH Image to ImageJ: 25 years of image analysis, Nat. Methods. 9 (2012) 671–675. doi:10.1038/nmeth.2089.

[23] M.D. Abramoff, P.J. Magalhães, S.J. Ram, Image processing with ImageJ, Biophotonics Int. 11 (2004) 36–42. http://dspace.library.uu.nl/handle/1874/204900 (accessed May 13, 2016).

[24] D. Woodley, Personal Communication, (2018).

[25] J. Ribis, S. Lozano-Perez, Orientation relationships and interface structure of α-Cr nanoclusters embedded in α-Fe matrix after α-α' demixing in neutron irradiated Oxide Dispersion Strengthened material, Mater. Lett. 74 (2012) 143–146. doi:10.1016/j.matlet.2012.01.115.